Gulley, A. K., Eccles, J. D., Kaipio, J. P., Malin, P. (2017): The effect of gradational velocities and anisotropy on fault-zone trapped waves. - *Geophysical Journal International*, *210*, 2, pp. 964—978.

DOI: http://doi.org/10.1093/gji/ggx200

Geophysical Journal International

Geophys. J. Int. (2017) **210,** 964–978
Advance Access publication 2017 May 10
GJI Seismology

doi: 10.1093/gji/ggx200

The effect of gradational velocities and anisotropy on fault-zone trapped waves

A.K. Gulley,[1] J.D. Eccles,[2] J.P. Kaipio[1,3] and P.E. Malin[4,5]

[1]*Department of Mathematics and Dodd-Walls Centre, University of Auckland, Private Bag* 92019, 1142 *Auckland, New Zealand.*
E-mail: anton.gulley@auckland.ac.nz
[2]*School of Environment, University of Auckland, Private Bag* 92019, 1142 *Auckland, New Zealand*
[3]*Department of Applied Physics, University of Eastern Finland, P.O. Box* 1627, *FI-*70211 *Kuopio, Finland*
[4]*Department of Physics, University of Auckland, Private Bag* 92019, 1142 *Auckland, New Zealand*
[5]*GFZ German Research Center for Geosciences, Telegrafenberg, D-*14473 *Potsdam, Germany*

Accepted 2017 May 9. Received 2017 April 27; in original form 2016 October 12

SUMMARY

Synthetic fault-zone trapped wave (FZTW) dispersion curves and amplitude responses for F_L (Love) and F_R (Rayleigh) type phases are analysed in transversely isotropic 1-D elastic models. We explore the effects of velocity gradients, anisotropy, source location and mechanism. These experiments suggest: (i) A smooth exponentially decaying velocity model produces a significantly different dispersion curve to that of a three-layer model, with the main difference being that Airy phases are not produced. (ii) The FZTW dispersion and amplitude information of a waveguide with transverse-isotropy depends mostly on the Shear wave velocities in the direction parallel with the fault, particularly if the fault zone to country-rock velocity contrast is small. In this low velocity contrast situation, fully isotropic approximations to a transversely isotropic velocity model can be made. (iii) Fault-aligned fractures and/or bedding in the fault zone that cause transverse-isotropy enhance the amplitude and wave-train length of the F_R type FZTW. (iv) Moving the source and/or receiver away from the fault zone removes the higher frequencies first, similar to attenuation. (v) In most physically realistic cases, the radial component of the F_R type FZTW is significantly smaller in amplitude than the transverse.

Key words: Numerical modelling; Guided waves; Seismic anisotropy; Fractures, faults, and high strain deformation zones.

1 INTRODUCTION

Mature fault zones are narrow regions (metres to kilometres wide) within the Earth's crust that represent zones of localized strain accommodating earthquake processes (Ben-Zion & Sammis 2003). Fault zones are developed by these earthquake processes and therefore understanding fault zones can provide understanding of past earthquakes and their mechanics (Dor *et al.* 2006; Ben-Zion & Ampuero 2009; Faulkner *et al.* 2011; Savage & Brodsky 2011; Xu *et al.* 2012). Mature fault zones typically have a high along-fault permeability which may penetrate to some depth and so play an important role in the movement of crustal fluids (Faulkner *et al.* 2011). They are also significant for the distribution of economically important minerals (e.g. Weatherley & Henley 2013) and the flow of fluids in hydrocarbon reservoirs (e.g. Ali *et al.* 2011). Fault zones contain information on future rupture dynamics including the style of earthquake rupture, slow slip or creep (Peng & Gomberg 2010). These clues can come from numerous sources, including the frictional properties of the principal slip zones (den Hartog *et al.* 2012; Haines *et al.* 2014) and the current seismology (Ellsworth *et al.* 2007).

Geologic investigations into fault zones provides information on rock properties in the near surface (Faulkner *et al.* 2010) and drilling allows for further investigations from a borehole (e.g. Zoback *et al.* 2011). These can be complemented by geophysical methods which can be used to make inferences about *in situ* geologic and fluid properties to greater depth or rock volume. These methods can range from exploration to monitoring, gravity to seismic. Fault zones can be geodetically identified and modelled using InSAR and GNSS data before and after earthquakes (e.g. Fialko *et al.* 2002; Lindsey *et al.* 2014). Gravity, exploiting low density fault zones, has also been used to image fault zones (Mooney & Ginzburg 1986; Chester *et al.* 1993; Cochran *et al.* 2009) however non-uniqueness means estimating fault-zone properties at depth is difficult. Seismic methods of increasing sophistication are utilized. Ambient noise measurements using a dense array placed around a fault zone have been used to calculate Green's functions through cross-correlation (e.g. Lin *et al.* 2013; Zhang & Gerstoft 2014), achieving a

resolution of approximately 100 m to depths of 1 km (Lin *et al.* 2013). All of these methods can provide characterization of fault zones in the upper few kilometres. It is also desirable to understand fluid flow path ways, strain localization and deformation at greater depths (Ben-Zion & Sammis 2003). Microseismicity, body, surface, head and trapped waves contribute to this (e.g. Ben-Zion & Malin 1991; Eberhart-Phillips & Michael 1993; Boese *et al.* 2012; Ben-Zion *et al.* 2015; Hillers & Campillo 2016). Fault-zone trapped waves (FZTWs) are focussed in for this study.

FZTWs are seismic energy that is guided by the low velocity zone of a mature fault through total internal reflection. Three different modes of FZTWs have been observed. The F_L FZTWs are analogous to Love mode surface waves. These are made up entirely of shear waves (*S*-waves) and have fault-parallel polarization that is orthogonal to the direction of travel (radial direction). This is also known as *SH* motion. The first reported observations of F_L in a fault zone were in controlled source surface-to-borehole studies at Oroville, California (Leary *et al.* 1985, 1987; Li & Leary 1990; Li *et al.* 1990). The F_R FZTWs are analogous to Rayleigh mode surface waves (Malin & Lou 1996). Most of the F_R energy propagates as *S*-waves with a smaller proportion of the energy propagating as Primary waves (*P*-waves). They have radial and fault orthogonal polarization which is also known as *P–SV* motion. While the F_L and F_R FZTWs are observed as dispersive coda arriving after the *S*-wave, F_ϕ waves arrive between the *P*- and *S*-wave direct arrivals. The F_ϕ are a leaky wave type FZTW that are only partially trapped by the waveguide. Like the F_R, F_ϕ have *P–SV* polarization. However, the F_ϕ energy is dominated by *P*-waves and energy leaks from the waveguide in the form of *S*-waves. These were first observed in passive source experiments on the San Andreas Fault (Ellsworth & Malin 2011). Identification and modelling of these different FZTW phases provides the potential for increased discrimination of detailed fault-zone properties such as anisotropy by exploiting differing polarization.

FZTWs are primarily used for the imaging and understanding of fault zones. They have been used to estimate the across-fault properties of a low velocity zone at a resolution of tens of metres (Ben-Zion *et al.* 1992, 2003; Hough *et al.* 1994; Haberland *et al.* 2003, 2007; Li *et al.* 1997, 1998, 1999, 2014; Li & Vernon 2001; Li & Malin 2008; Mizuno *et al.* 2004; Lewis *et al.* 2005, 2007; Wu *et al.* 2010; Ellsworth & Malin 2011; Eccles *et al.* 2015). Several different analytical, numerical and computational approaches have been proposed and employed to investigate the effects of 2-D and 3-D variations in rock properties, source type and location. In the following we give a brief review of these approaches and findings.

2-D finite difference modelling of F_L was done in Li & Vidale (1996). They demonstrated that in order to observe an FZTW, the fault zone must be approximately continuous between the source and the receiver and that the earthquake must have occurred within a few fault-zone widths of the fault. They also showed that many 2-D structural variations within the fault zone such as bending, moderate changes in fault-zone widths and bifurcating faults cause a reduction in FZTW energy but do not prevent them from being observed.

The analytic solution for two dimensional F_L waves for a fault zone made of homogenous layers was derived by Ben-Zion (1990) and Ben-Zion (1998). They showed that increasing velocity contrast between the fault and country-rock increases the trapping efficiency of the waveguide. There are significant trade-offs between fault-zone width, propagation distance along the fault and velocity contrast which means that a variety of different fault-zone models can produce the same or similar FZTWs.

Two-dimensional finite difference modelling of both F_L and F_R FZTWs were compared to analytical solutions by Igel *et al.* (1997). They discovered that rapid changes in the *S*-wave velocity model with depth that is greater than the fault zone to country-rock velocity contrast can destroy FZTWs. On the other hand, a geologically expected fault zone widening at the surface has only a small effect on the waveform, while random perturbations in the velocity model that are smaller than the velocity contrast have no significant effect on the waveform (Igel *et al.* 1997).

The depth extent of low velocity zones has proven controversial. Numerous studies have suggested that the low velocity zone persists for greater than 10 km, which is approximately the entire seismogenic zone (e.g. Li *et al.* 2000, 2002, 2004; Li & Vernon 2001). Other researchers, utilizing some of the same or similar FZTW data, have proposed that the low velocity zone terminates at a much shallower 5 km depth or less (e.g. Ben-Zion & Sammis 2003; Ben-Zion *et al.* 2003; Peng *et al.* 2003; Fohrmann *et al.* 2004; Lewis *et al.* 2005). Part of the difficulty in determining the depth is because of the high level of uncertainty and non-uniqueness associated with FZTWs (Michael & Ben-Zion 1998). This means that different fault-zone models can produce the same or very similar waveforms. Another issue is that it is difficult to determine if seismic waves are entering the fault zone from beneath or tunnelling in higher up in a fault zone (Wu 2008). Given these apparent limitations of FZTWs, other methods have potentially been more successful in determining the depth of fault zones. Refracted and reflected *P*- and *S*-waves can be used to infer the depth extent and properties of fault zones (Yang & Zhu 2010; Yang *et al.* 2011, 2014). These studies have demonstrated that the Calico and San Jacinto fault zones are shallow.

Three-dimensional finite difference modelling of FZTWs was followed by Igel *et al.* (2002) and Jahnke *et al.* (2006). They showed that, in general, infinite 2-D line sources can not be used to approximate 3-D point sources for FZTW. However, applying an approximate 3-D to 2-D conversion to the data can be used to make this approximation feasible in some cases. They also showed that 3-D velocity variations that are smaller than the velocity contrast between the fault and country-rocks overprinting on a 2-D structure do not significantly affect the recorded FZTW coda and that the other observed 2-D effects mentioned above still hold in the 3-D case.

The sensitivity of fault zones to *P*-, Head and FZTWs was analysed in Allam *et al.* (2015) using finite-frequency sensitivity kernels. Their methods used 3-D full waveform modelling via the spectral element method (Komatitsch & Tromp 1999) and sensitivity was computed using the associated adjoint method (Tromp *et al.* 2005). The results in Allam *et al.* (2015) demonstrate the similar properties that FZTWs have with surface waves and that fault zones are less sensitive to *P*-waves compared to the Head and FZTWs. The spectral element method used allows for investigation of gradational across-fault velocity models and it was also demonstrated that gradational across-fault velocity models do not significantly change the sensitivity pattern of FZTWs.

Geological observations of fault zones have revealed that different mature fault zones vary considerably (Ben-Zion & Sammis 2003; Faulkner *et al.* 2010; Yang 2015). The effective widths of mature low velocity zones are thought to range on the scale of metres to kilometres (Ben-Zion & Sammis 2003). There is also significant variation of seismic properties within a fault zone (Faulkner *et al.* 2011; Savage & Brodsky 2011; Yang 2015). The low velocity waveguide is commonly attributed to the fracture damage zone of the fault caused by past events (Dor *et al.* 2006; Ben-Zion & Ampuero 2009; Faulkner *et al.* 2011; Xu *et al.* 2012). The

across-fault profile of the fault might therefore be expected to have a velocity model that behaves in an exponential or power law fashion (Leary *et al.* 1987; Li & Vidale 1996; Mitchell & Faulkner 2009; Savage & Brodsky 2011; Johri *et al.* 2014).

Despite these geologic and numerical observations, a widely used approximation is that a fault zone can be thought of as a single layer of low velocity rock surrounded by intact rock (Ben-Zion & Aki 1990; Li *et al.* 1990, 1998; Mizuno & Nishigami 2006; Wu *et al.* 2008; Lewis & Ben-Zion 2010; Calderoni *et al.* 2012; Eccles *et al.* 2015). These approximations are made because, such a three-layer model is computationally straightforward to implement (Ben-Zion & Aki 1990) and allows for a simple comparison between different fault zones. A five-layer extension for the three-layer model was used with finite difference modelling in Li & Malin (2008). The spectral element method (Komatitsch & Tromp 1999) can be used to account for these gradational across-fault properties. This has been done by Allam *et al.* (2015) to compute sensitivity kernels and it was shown that fault-zone properties may be inferred by FZTW measurements for both gradational and layered across-fault velocity models. However, no comprehensive studies yet exist into how a layered versus gradational across-fault velocity model affects the properties of FZTWs.

One of the main goals of this study is to provide an understanding of the properties of FZTWs propagating in a gradational velocity model. This is in order to show the differences between a gradational and layered velocity model and why it is important to consider the across-fault velocity model. In particular we show that FZTWs travelling in a simple gradational velocity model have a significantly shorter wave-train and lack an Airy phase compared to the equivalent three-layer model.

Due to preferential alignment of fractures and parallel layering, fault zones are generally considered to be anisotropic (Leary *et al.* 1987; Li *et al.* 1987; Cochran & Vidale 2001). In many cases, this anisotropy can be approximated by assuming transverse-isotropy, which means that rays travelling parallel to the principal fault plane have the same velocity (Leary *et al.* 1987; Li *et al.* 1987). Anisotropy in waveguides has been widely explored in the context of coal seam seismics (Lou & Crampin 1991; Buchanan *et al.* 1983). They showed that the dispersion curve of an anisotropic waveguide is similar to an isotropic waveguide but the precise numerical values of group velocity and phase velocity differ. Furthermore, Nakamura & Takenaka (2006) used a matrix propagator method to simulate FZTWs in a 2-D homogeneous transversely isotropic waveguide surrounded by isotropic country-rock. These synthetic earthquakes are located beneath an array of seismometers. They performed a Shear wave splitting analysis to the synthetic waveforms and concluded that anisotropy can be detected when the focal mechanisms of the earthquake are dip-slip but not when they are strike-slip.

While these studies have provided useful information in their respective areas, no study has investigated how anisotropy affects trapped waves in the context of using them for imaging a fault zone. In this study we investigate how a simple 1-D transversely isotropic velocity model affects FZTWs as well as the relative importance of the respective anisotropy parameters. We also show that a transversely isotropic fault zone has F_L arrivals with a shorter wave-train than F_R.

In addition to investigating gradational velocity models and transverse anisotropy we also reinvestigate the effect of source/detector locations with respect to the fault zone and the implications of the focal mechanism to the modelled FZTWs. These investigations are done using a finite element solver that efficiently finds the trapped modes, dispersion curves, amplitude responses and full waveforms of FZTWs. This solver is limited to transversely isotropic velocity models that can change in the across-fault direction only.

2 COMPUTATIONAL APPROACH OVERVIEW

The methodology discussed in Gulley *et al.* (2017) is used for the computation of the FZTW responses. This method starts with the 3-D transversely isotropic elastic wave equation (Aki & Richards 2009) and assumes that the velocity model is varying in the across-fault (z) direction only and that the wave is travelling in the $x-z$ plane. Therefore, the Fourier substitution of $\boldsymbol{u} = \tilde{\boldsymbol{u}}\exp(ikx - i\omega t)$ can be made, where $\boldsymbol{u}$ is displacement, $\tilde{\boldsymbol{u}}$ is displacement amplitude, i is the imaginary number, k is the wave number, x is the radial direction, ω is angular frequency and t is time. The resulting is a Helmholtz type, second order system of differential equations in z. The differential equations can be approximated using a higher order finite element method which can also be referred to as the spectral element method (Komatitsch & Tromp 1999). The equations can then be rewritten as two decoupled matrix eigenvalue equations with k or ω as the eigenvalue and a form of $\tilde{\boldsymbol{u}}$ as the eigenvector. These two decoupled equations relate to the F_L (Love) and F_R (Rayleigh) FZTWs. Numerically solving the eigenvalue equations for different values of phase speed ($c = \omega/k$) allows the dispersion curves to be calculated. The group velocities, amplitude responses and reconstructed waveforms can then be computed using the energy integral methods defined in Aki & Richards (2009). This solver can efficiently handle arbitrary gradational transversely isotropic velocity models allowing them to be easily investigated. It also allows for separate computation of dispersion curves and can compute the FZTW waveform from different source types including a moment tensor point source.

3 ISOTROPIC MODELS: GRADATIONAL VELOCITIES, SOURCE LOCATIONS AND FZTW PARTITIONING

1-D isotropic velocity models are used to investigate the effects on modelled FZTWs of gradational versus layered velocity models, the dependence on source and receiver locations, the relative amplitudes of the F_L or F_R components and the dependence of these components on the direction of the earthquake slip vector. The coordinate system and displacement directions are shown in Fig. 1.

3.1 Gradational versus layered velocity profiles in the fault zone

In order to investigate the effect of gradational velocity models we compute the dispersion and amplitude response of three different velocity model types. The velocity models are a three-layer model, a five-layer model and an exponentially decaying (1/cosh) model. The three-layer model is chosen because it is very commonly used (e.g. Li *et al.* 1990, 1997; Hough *et al.* 1994; Mizuno & Nishigami 2006; Mizuno *et al.* 2008; Wu *et al.* 2010). The five layer model, which begins to approximate more complex or gradational velocity models has been previously used (e.g. Li & Malin 2008). While any number of gradational velocity models could have also been used and our investigations showed that the 1/cosh model has similar waveforms and dispersion curves to Gaussian approximations, the smoothly varying and exponentially decaying 1/cosh

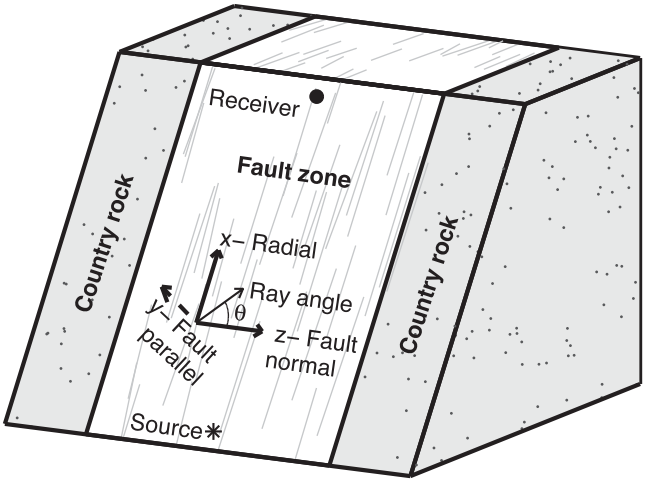

Figure 1. Setup of the fault-zone and coordinate system used. The direction x is pointing directly from source to receiver, parallel to the fault. The direction z is normal to the fault and y is the remaining direction in the right hand co-ordinate system. All FZTWs have energy travelling in the x direction. The *P–SV* displacement is in the x–z plane. This corresponds to the F_R FZTW with the F_R radial displacement being in the x direction and the F_R transverse displacement in the z direction. The F_L FZTWs have displacement in the y direction. The ray angle defined here is used in Section 4.

model additionally approximates geologically expected fracture patterns (Savage & Brodsky 2011). A very low spatial attenuation of $Q_\alpha = Q_\beta = 1000$ has also been used in each velocity model. These velocity models, amplitude responses and the group velocities of the two lowest harmonics of the F_L and F_R FZTWs are shown in Fig. 2. It can be seen that the three-layer and the five-layer velocity models have significantly different dispersion curve character to the exponentially decaying velocity model. The group velocities of the three- and five-layer models have local minima below the minimum velocity of the waveguide (the Airy phase) and even lower group velocities are seen in higher harmonics. On the other hand, the exponentially decaying velocity profile does not exhibit an Airy phase. The exponentially decaying velocity model has a minimum group velocity which is close to the minimum velocity of the waveguide for all harmonics. Lower minimum group velocities lead to increased wave-train/coda length. The five-layer model gives a reasonable approximation of the exponentially decaying model only at low frequencies, albeit with lower amplitude responses.

The velocity profile can also result in different trapping efficiencies. The three-layer model traps up to 20 per cent more seismic energy than the exponentially decaying (1/cosh) waveguide as seen in Fig. 2. The amplitude responses shown represent the amplitude of each frequency component and shows how well each frequency is trapped by the waveguide.

3.2 Varying source and receiver locations in the fault-perpendicular direction across the fault zone

Different source/receiver locations can affect the amplitude response of FZTWs. In particular, we are interested in how close to the fault zone a source/receiver needs to be to generate/observe FZTWs. We note that keeping the receiver in a constant location and moving the source is approximately equivalent to keeping the source constant and moving the receiver which can be seen through analysis of the surface wave functions in Aki & Richards (2009). The topic of source and receiver locations was first investigated using an analytic solution for FZTWs in a layered medium by Ben-Zion & Aki (1990). Later, 2-D finite difference modelling was done by Li & Vidale (1996) and finite-frequency sensitivity kernels were computed by Allam *et al.* (2015). These researchers suggested that FZTWs can be observed when the source and/or receiver is located within three fault widths from the centre of the fault. Here, we compute the amplitude responses for the fundamental and the first harmonic and show their dependence on the source location. In particular, we investigate the influence source/recover location has on which frequencies are trapped/recorded.

The amplitude responses and the corresponding waveforms associated with three infinite line sources that are located at increasing distances away from the fault zone are shown in Figs 3 and 4, respectively. These figures indicate that moving the source away from the fault zone causes a reduction in trapped amplitude at all frequencies but the higher frequencies are removed over the shortest propagation distance. The corresponding eigenmodes are shown in Fig. 5. These eigenmodes represent the amplitude of the wave for each frequency as it travels along the waveguide (Gulley *et al.* 2017). This removal of the higher frequencies occurs because the lower frequency trapped modes penetrate further into the country-rock as indicated by Fig. 5. Anelastic attenuation also causes the reduction of higher frequencies faster than low frequencies. This means that, when imaging fault zones using FZTWs, there is a significant trade-off between the anelastic attenuation parameter 'Q' and the location of the source across the fault zone. Both of these parameters significantly affect the amplitude of the FZTW and have only a minor effect on the dispersion of the wave. This means that the influence of these two parameters can be significantly reduced when modelling FZTWs by considering the dispersion.

3.3 Relative amplitudes of FZTW components

FZTWs can cause displacement in all three directions (see Fig. 1). These components often contain different amounts of energy. This can be understood by looking at the resonant waveforms of the waveguide (eigenvectors). The resonant waveforms correspond to free oscillations in the waveguide at a fixed frequency. Examples of different resonant waveforms are shown in Fig. 5. In what follows, 'radial' refers to particle motion that is oriented along the line between source and receiver while 'transverse' refers to motion that is perpendicular to this direction, as shown in Fig. 1. The results show that the radial component of the F_R resonant waveform is significantly smaller than the transverse component. This is because the F_R resonant waveform is dominated by *S*-waves while the *P*-waves propagate in an evanescent form (following the definitions of Kennett 1983; Chapman 2004). For example, there is ∼8 times the amount of kinetic energy in the shearing motion (*S*-wave) than in the compressional motion (*P*-wave) of the 15 Hz trapped F_R fundamental resonant waveforms as seen in Fig. 5. As the FZTW propagates predominantly in the radial direction, the transverse component contains most of the *S*-wave energy while the radial component contains the majority of the *P*-wave energy. The result is that the radial component of the full F_R waveform can be expected to be significantly lower in amplitude than the transverse component as shown in Figs 3 and 4. This can be observed in FZTWs produced on the Alpine Fault (Eccles *et al.* 2015).

The exception to this rule is if the *P*-wave velocity of the fault zone is less than the *S*-wave velocity of the country-rock. In such a case, the *P* component would not propagate as an evanescent

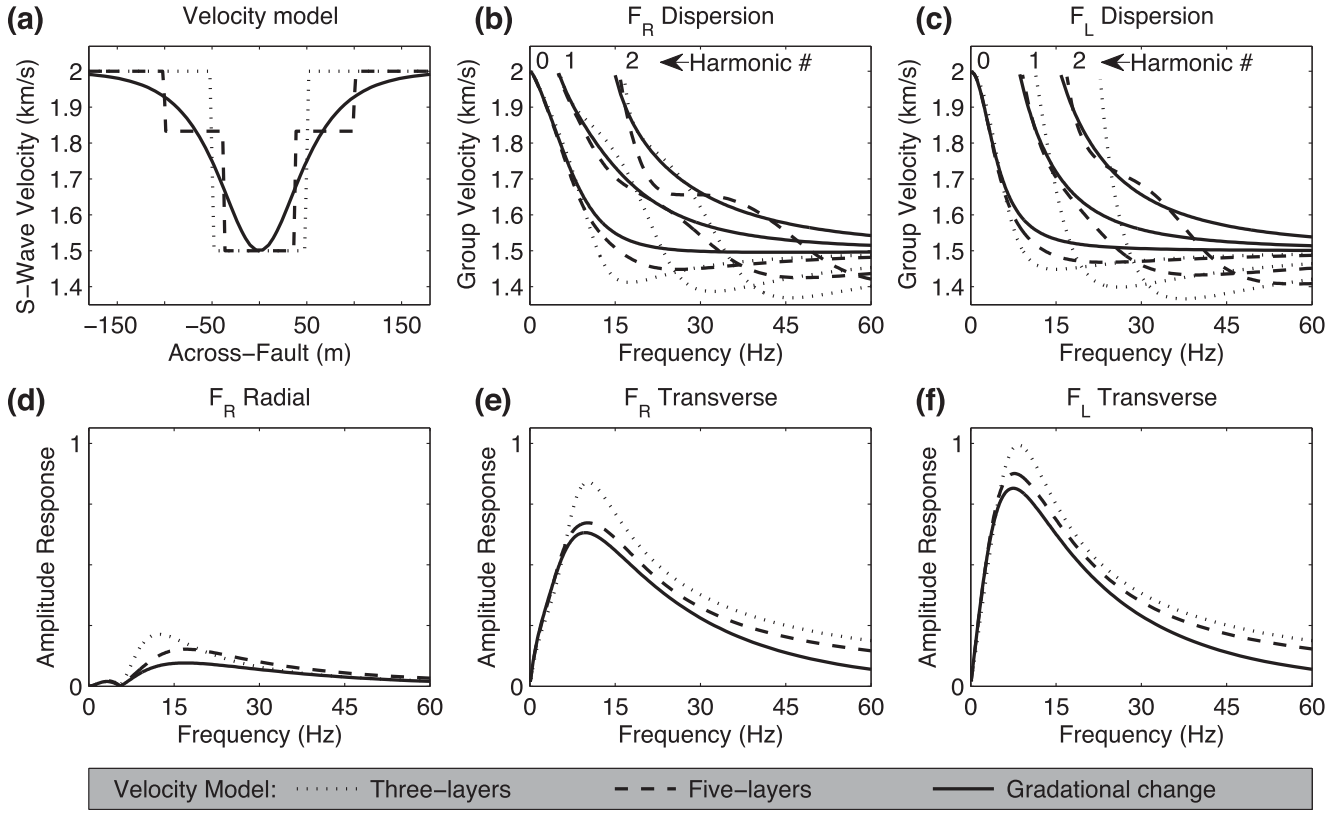

Figure 2. (a) The three isotropic velocity models. The exponential decay model is a 1/cosh function. The elastic values and boundaries of the three-layer and five-layer stratified fault-zone models are chosen so that they are least-squares approximations to the exponential velocity model. The effective width of all three models equals 100 m. Only the *S*-wave velocities are shown; the *P*-wave velocities and density profiles have the same shape with minimum and maximum values of 2.85–3.2 km s^{-1} and 2600–2700 kg m^{-3}. (b,c) The F_L and F_R dispersion curves for the fundamental and the lowest two harmonics, respectively. The exponential velocity model has qualitatively different dispersion to the layered velocity models. In particular, the exponentially decaying model does not exhibit an Airy phase (a local minimum). (d–f) The amplitude responses of the fundamental generated by an isotropic infinite line source that is an impulse function in time. The source and receiver are both offset 25 m from the fault centre and the radial distance from source to receiver is 10 km. The radial direction refers to the direction oriented along-fault between the source and the receiver. The F_R transverse component has displacement perpendicular to the fault plane and the F_L component has displacement parallel with the fault plane. A very low spatial attenuation of $Q_\alpha = Q_\beta = 1000$ is assumed.

wave and the guided wave would therefore no longer be dominated by the *S*-wave energy. However, such a situation is unlikely as the maximum country-rock to fault rock *S*-wave velocity ratio that has been estimated is 1.6 (Haberland *et al.* 2003) which is less than the fault rock *P*-wave to *S*-wave velocity ratios recorded in fault zones around the world (Li *et al.* 2004; Hung *et al.* 2009).

The shape of the trapped modes is similar for the F_L mode and the transverse component of the F_R mode as shown in Fig. 5. This is because the F_L mode is made up of shearing motion only and the F_R mode's transverse component is shearing dominated, as discussed above.

The trapped modes shown in Fig. 5 also indicate that the F_R radial components of the fundamental have a zero near the middle of the fault, which is where the F_R transverse component and F_L exhibit their highest amplitudes. Thus, recording FZTWs in the centre of the fault zone will maximize the signal to noise ratio of the transverse components of the fundamental FZTWs but will result in the radial component having a smaller amplitude.

3.4 Orientation of the slip vector to the receiver

This section looks at the source–receiver orientation for an earthquake with a moment tensor point source. We assume here that the earthquake slip vector lies on the plane at the centre of the fault zone. When the earthquake slip vector is aligned with the source-receiver direction (0° or 180° in Fig. 6), only the F_R mode is generated in those directions, that is, F_L is not seen. This is because with this slip vector there is little energy generated in the direction in which F_L waves are polarized. Correspondingly, when the slip vector is perpendicular to the source–receiver direction (90° in Fig. 6), only the F_L mode is recorded at the receiver. The implications are that in some cases, focal mechanisms may need to be taken in to account when modelling FZTWs. This also means that FZTWs could possibly be used in the future to assist in the estimation of focal mechanisms, provided there are multiple seismometers that are spaced sufficiently far apart along the fault zone to capture a large range of different angles to the source. Note that these results do not necessarily hold for FZTW sources that are below a fault zone.

4 ANISOTROPY

Fault zones are expected to be anisotropic due to preferential alignment of fractures and fault-parallel layering of rock beds (Leary *et al.* 1987; Li *et al.* 1987; Cochran & Vidale 2001). Many fault zones can be assumed to be transversely isotropic if the fractures and/or bedding are aligned parallel to the fault plane

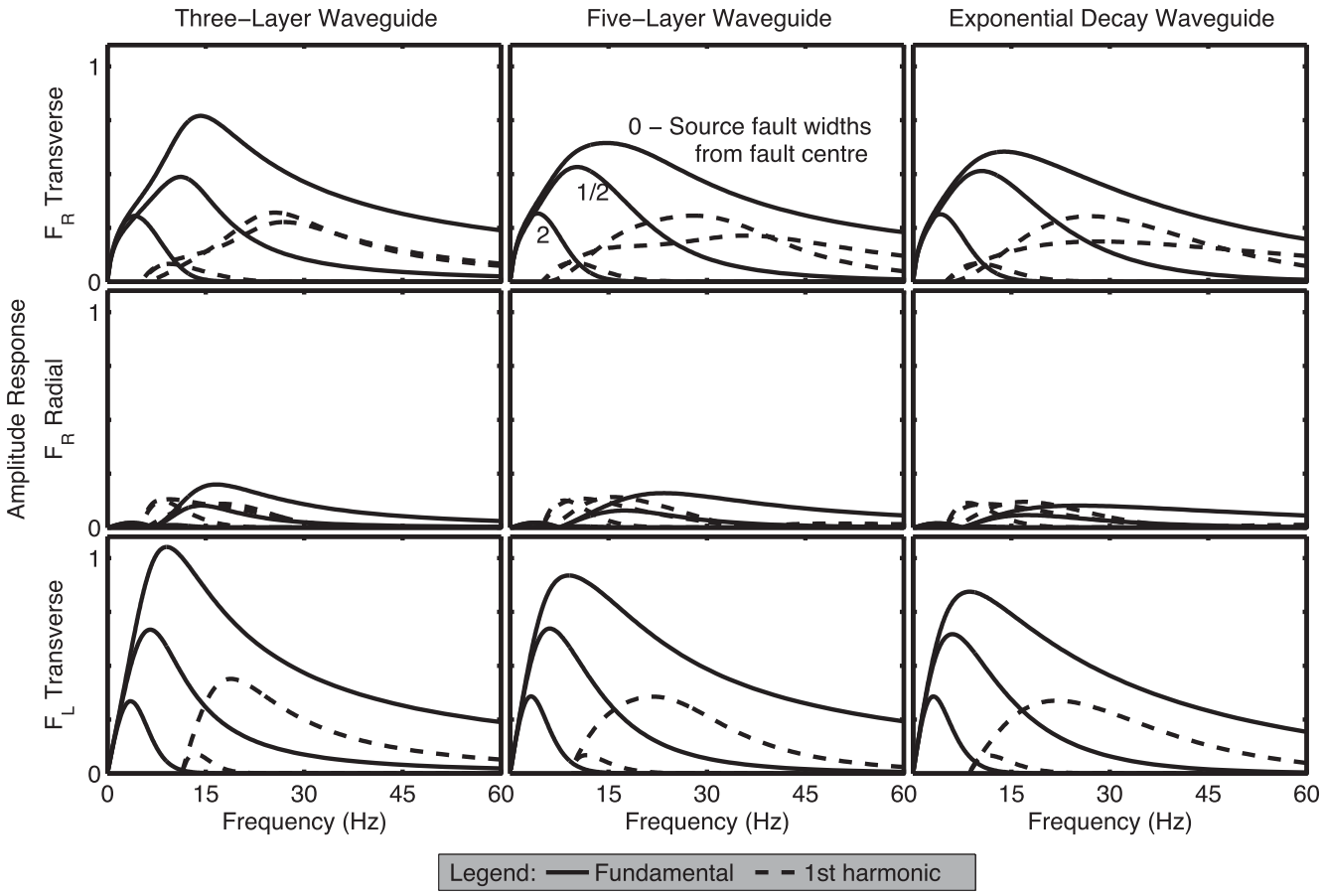

Figure 3. Amplitude responses for the velocity models shown in Fig. 2(a) for different source (or receiver) offsets from the fault centre. The sources are located 10 km along-fault from the receiver and the fault-perpendicular offsets of the five sources from the fault are 0, 1/2 and 2 fault widths (100 m) from the fault centre. These offsets are indicated in the top middle subplot. All sources are isotropic infinite line sources (2-D) with a temporal impulse and the receiver is offset from the fault centre by 1/4 of the fault-zone width (25 m). While this figure investigates different source positions, moving the source position is equivalent to moving the receiver position (for the source type used) and this figure can also be viewed as amplitude responses on an across-fault array of seismometers from a single source position. Here, we have assumed very low spatial attenuation of $Q_\alpha = Q_\beta = 1000$. It can be seen that the effect of moving the source/receivers away from the fault zone removes high frequencies. It is also seen that the radial component has complex behaviour and is generally much lower in amplitude (also see Fig. 5).

(Leary *et al.* 1987). Here we investigate the effects of transverse-isotropy on FZTWs.

4.1 Parameterization of anisotropy

We assume that the fault plane is the x–y plane and that this is the plane of transverse-isotropy. Without loss of generality, we can therefore take wave propagation directions to be only in the x–z plane. Fig. 1 shows the propagation angle θ that describes a ray angle in the x–z plane with $\theta = 0^\circ$ meaning propagation in the z direction and $\theta = 90^\circ$ being propagation in the x direction. In this situation, the P-waves have particle displacement in the x–z plane only and we denote the respective velocity by α. The S-waves with particle displacement in the x–z plane have velocities denoted β^{V} and S-waves with particle displacement in the y direction only have velocity β^{H}.

To investigate the effects of anisotropy on FZTWs we make use of the parametrization of transverse-isotropy as defined in Thomsen (1986). These parameters are α_0, β_0, ϵ, γ, δ. The α_0 and β_0 are the P- and S-wave velocities in the z-direction. The parameters ϵ and γ describe the anisotropy of the P- and SH-velocities, respectively, and δ is a further parameter related to P- and SV-wave velocities. The velocity of a particle $\alpha(\theta)$ propagating at an angle θ and its relationship to the other parameters were derived in Thomsen (1986) as:

$$\alpha(\theta) = \alpha_0 \left[1 + \epsilon \sin^2(\theta) + D^*(\theta)\right]^{1/2}, \tag{1a}$$

$$\beta^{\mathrm{V}}(\theta) = \beta_0 \left[1 + \alpha_0^2 \beta_0^{-2} \epsilon \sin^2(\theta) - \alpha_0^2 \beta_0^{-2} D^*(\theta)\right]^{1/2}, \tag{1b}$$

$$\beta^{\mathrm{H}}(\theta) = \beta_0 \left[1 + 2\gamma \sin^2(\theta)\right]^{1/2}, \tag{1c}$$

$$D^*(\theta) = \frac{\left(1 - \beta_0^2 \alpha_0^{-2}\right)}{2} \left(\left[1 + \frac{4(2\delta - \epsilon)}{1 - \beta_0^2 \alpha_0^{-2}} \sin^2(\theta) \cos^2(\theta) + \frac{4\epsilon \left(1 - \beta_0^2 \alpha_0^{-2} + \epsilon\right)}{\left(1 - \beta_0^2 \alpha_0^{-2}\right)^2} \sin^4(\theta) \right]^{1/2} - 1 \right). \tag{1d}$$

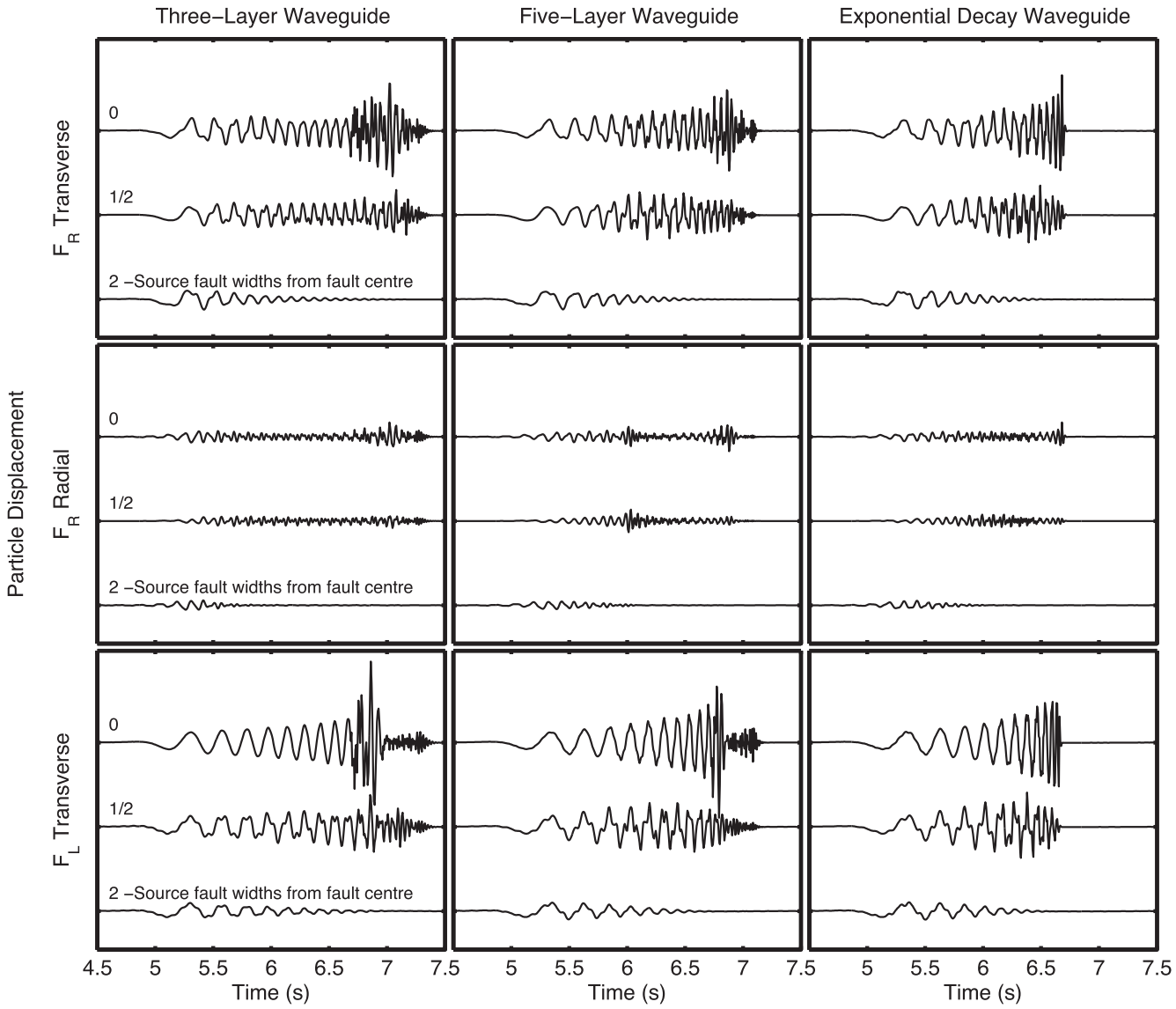

Figure 4. The observed waveforms generated by the amplitude responses and source types shown in Fig. 3. The corresponding velocity models and dispersion curves are shown in Fig. 2. The three source positions used are when the source is offset: 0 (top), 1/2 (middle) and 2 (bottom) fault widths (100 m) in the fault-perpendicular direction from the fault centre as indicated in the first column of subplots. While this figure investigates different source positions, moving the source position is equivalent to moving the receiver position (for the source type used). This figure can thus also be viewed as waveforms recorded on an across-fault array of seismometers from a single source position. The exponential decay waveguide exhibits a shorter wave train with frequency increasing monotonously with time. The fundamental and all harmonics of the exponentially decaying waveguide finish at a single point in time that corresponds to propagation distance divided by minimum velocity of the waveguide (6.7 s = 10000 m /1500 m s^{-1}). The three- and five-layer velocity models have some differences in their FZTW behaviour. There is a maximum amplitude peak which corresponds to the Airy phase after which the lower amplitude higher harmonics can be observed. At approximately 6.7 s for the three- and five-layer waveguides, multiple frequencies from the same harmonic are recorded. This does not occur in the exponential decay waveguide.

From eqs (1), we have:

$$\alpha(0^\circ) = \alpha_0, \tag{2a}$$

$$\alpha(90^\circ) = \alpha_0(1+2\epsilon)^{1/2}, \tag{2b}$$

$$\beta^{\mathrm{V}}(90^\circ) = \beta^{\mathrm{V}}(0) = \beta^{\mathrm{H}}(0) = \beta_0, \tag{2c}$$

$$\beta^{\mathrm{H}}(90^\circ) = \beta_0(1+2\gamma)^{1/2}. \tag{2d}$$

4.2 Anisotropy in waveguides

As fault zones are known to be anisotropic we investigate how several geologically plausible fault zones will affect FZTWs. One situation is when the fault zone has fault-aligned fractures, foliation or lithologies (e.g. Leary *et al.* 1987). In this case, the F_R FZTW will have a longer wave-train and higher amplitude then the F_L. This is because the fault zone will have lower *SV* velocities than *SH* velocities, which increases the ability of the waveguide to trap *SV* waves and corresponds to lower minimum group velocities (longer wave-trains) and higher amplitude responses. This result can be seen in the anisotropic fault zone model in Fig. 7. In the

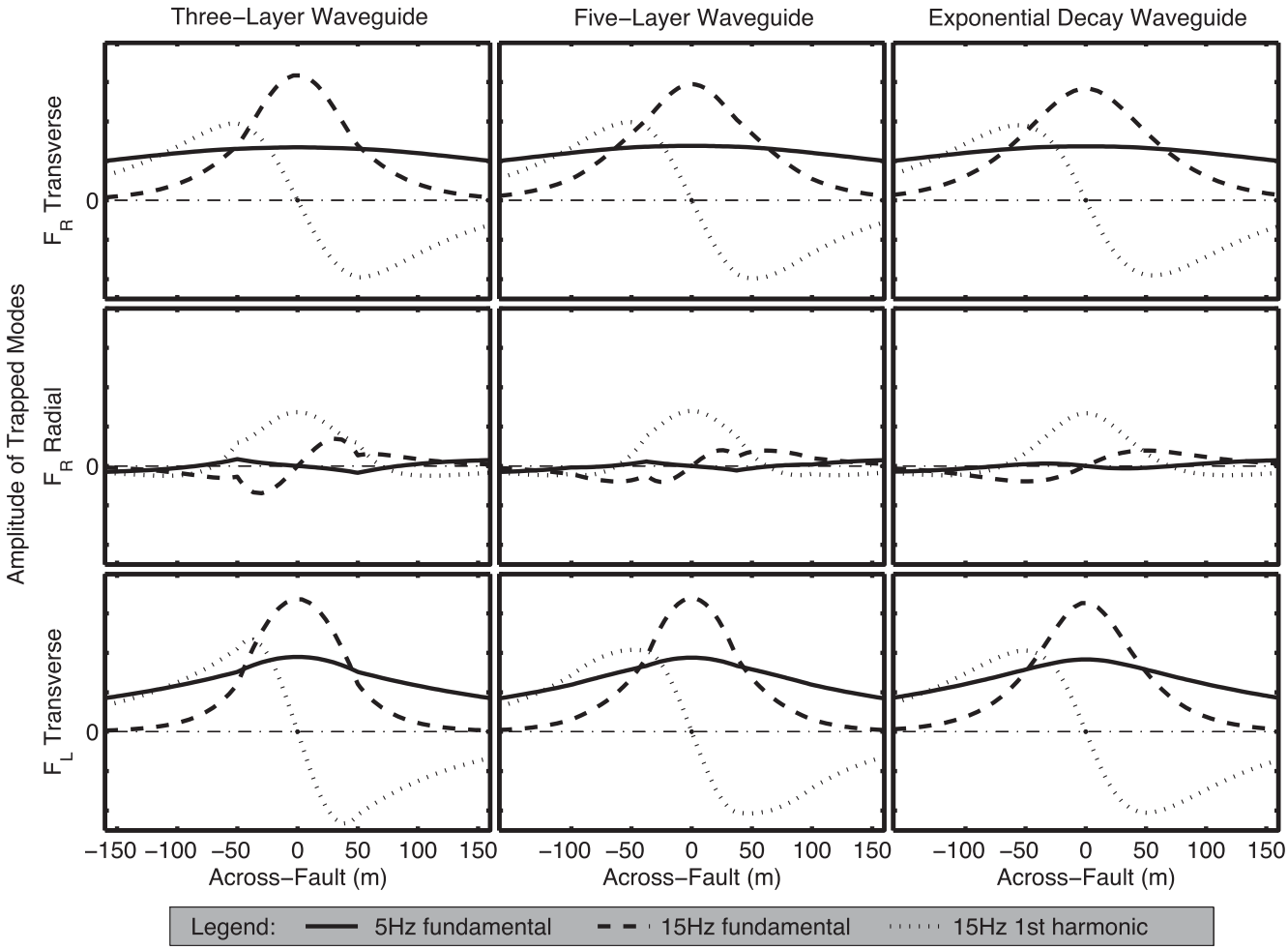

Figure 5. Three different resonant waveforms (waveguide eigenvectors) from the three different velocity models in Fig. 2. The waveforms are normalized by the respective kinetic energies and plotted on the same scale. The radial and transverse F_R resonant waveforms are coupled together. The F_R radial resonant waveform is significantly smaller in amplitude than the F_R transverse component. As the FZTW waveform is made up of all resonant waveforms, this implies that the radial part of the F_R guided wave should be significantly lower in amplitude than the transverse part. It can also be seen that, for the same harmonic, the lower frequencies penetrate further in the country-rock.

extreme case, in which the waveguide is almost entirely caused by anisotropy, there would be very little energy in the F_L as seen in Fig. 7. An alternative geologic model is an isotropic fault zone (e.g. unfoliated cataclasites) within a transversely isotropic country-rock (e.g. schist) which could be imagined from a structure such as New Zealand's Alpine Fault (Toy *et al.* 2015). In this case the *SV* velocities in the country-rock are lower than the *SH* velocities, resulting in reduced trapping for the F_R FZTW. The F_R therefore have a shorter wave train and lower amplitude as seen in Fig. 7.

4.3 Anisotropy approximations

In many cases in modelling we need to make assumptions or approximations due to insufficient knowledge or recourses. Here, we derive and investigate several high angle approximations to eqs (1). The aim of these approximations is to provide insight into the most important parameters for modelling FZTWs and to provide possible parameter reductions for modelling and inversions. We note that these approximations apply only to the fundamental (trapped) frequency. Guided waves are trapped when a propagating waves undergoes total internal reflection at each boundary (Ben-Zion 1998). The Snell's law for critical reflection angles shows that for guided waves to exist we must have

$$\theta \geq \theta_{\min} = \sin^{-1}\left(\frac{\min(\beta)}{\min(\beta(\pm\infty))}\right) = \sin^{-1}(1 - \text{velocity contrast}) \tag{3}$$

where $\theta_{\min}$ is the angle of propagation of the critically reflected ray at the location where β is smallest. This is the smallest possible angle of propagation for the FZTW.

Fault zones around the world have typically been modelled to have fault zone to country-rock velocity contrasts ranging between 5-50 per cent (Li *et al.* 1994; Ben-Zion *et al.* 2003; Mizuno & Nishigami 2006; Li & Malin 2008; Eccles *et al.* 2015). For small velocity contrasts, the inequality (3) suggests that the propagation angles on the x–z plane will be close to 90° (radial direction), and therefore taking a high angle approximation to eqs (1) is justified.

For larger velocity contrasts, the inequality (3) still suggests that the high angle velocities are significantly more important than the velocities in the direction orthogonal to the fault, since orthogonal rays are not trapped at all. In addition, a high degree of additional dependence on the velocities parallel to the fault is suggested by the fact that the range of possible trapped phase speeds depends only

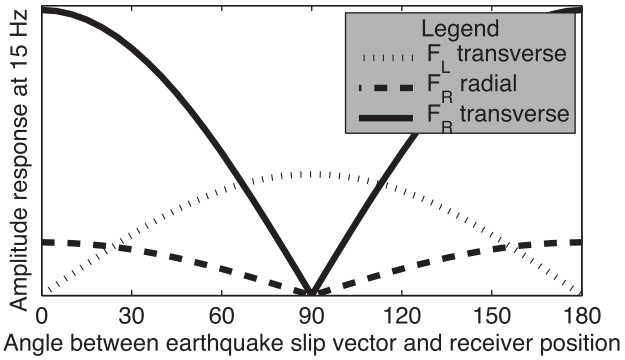

Figure 6. The amplitude response at 15 Hz (fundamental) of the 100 m wide three-layer model waveguide corresponding to Fig. 2(a). This amplitude response was generated from a moment tensor point source. The source and receiver are located at the edge of the fault zone (50 m). The earthquake slip vector is assumed to be on the same plane as the fault zone. The figure shows that when the earthquake slip vector is in the direction towards the receiver, only the F_R mode is generated. Correspondingly, when the slip vector is perpendicular to the direction towards the receiver only the F_L mode is generated. Similar results are produced by higher harmonics, different frequencies and different elastic models.

on these velocities (parallel to the fault) as shown by Gulley *et al.* (2017).

The upcoming approximations are made with only a few parameter sets of country-rock and fault zone α_0, β_0, ϵ, δ and γ. However, our testing has shown that these results generalize to other choices of these parameters.

4.3.1 *High angle approximation for the anisotropy parameter δ*

The anisotropy parameter δ influences $\beta^{\mathrm{V}}(\theta)$ and $\alpha(\theta)$ when $0^\circ < \theta < 90^\circ$ as is evident from eqs (1) and (2). The parameter can typically only be measured accurately with very specific apparatus such as the laser-based apparatus (Blum *et al.* 2013). Because of this difficulty in measuring δ, in many cases sufficient information on δ may not be available and so it needs to be approximated in some way.

For this outcome, we look for a high angle approximation to eqs (1). From these equations, it can be seen that as $\theta \to 90^\circ$ the term with $\cos^2(\theta)$ tends to zero suggesting that δ is negligible at high angles. If the anisotropy is due to thin layering of isotropic materials, then δ is less than the *P*-wave anisotropy parameter (ϵ) (Berryman 1979). In some cases, such as shale, $\delta > \epsilon$ but the bulk properties of most rock has $\delta < \epsilon$ (Thomsen 1986). In order to fulfil the requirement that the elastic parameter $C_{13} > 0$, δ needs to be greater than a small negative number (Thomsen 1986). Thus, choosing $\delta = \epsilon/2$ seems to be a feasible central choice for δ. Furthermore, setting $\delta = \epsilon/2$ makes the $\cos^2(\theta)$ term vanish in eqs (1).

As can be seen from eq. (1c), δ does not affect the *SH* velocities so we only need to test this approximation on the F_R guided waves. In order to do this, we continue to use the finite element method (Gulley *et al.* 2017; see Section 2) to compute the dispersion curves for $\epsilon = 0.15$ in the country-rock, $\epsilon = 0.3$ is the maximum value in the fault zone and $\delta = \epsilon/4$. This simulation is compared with a simulation using the approximation $\delta = \epsilon/2$ and the error in the approximation is taken as the difference between these two simulations. The values for ϵ used correspond to ∼25 per cent *P*-wave anisotropy in the fault zone and are realistic upper bounds (Thomsen 1986; Leary *et al.* 1987). The values α_0, β_0 and ρ are the same for all simulations in this section.

The first row of Fig. 8 shows different dispersion curves that are produced by this simulation for three different choices of the minimum value of β_0. It can be expected that this approximation is better at higher propagation angles. For a single dispersion curve, higher propagation angles correspond to higher frequencies and, as is seen in Fig. 8, the error is smaller at higher frequencies. The error is also less for smaller velocity contrast. This can be seen in the inequality (3) where a smaller velocity contrast leads to a minimum angle closer to 90°, hence the high angle approximation is better.

The errors are the greatest for the three-layer model and the smallest for the exponentially decaying model. This is because the exponentially decaying model and five-layer model have narrower regions where the velocity is equal to the minimum velocity. Using Snell's law, it can be seen that a ray moving to a faster region will have an increasing ray angle. This means that waves in the exponentially decaying model and five-layer model will spend more time propagating at higher angles which increases the validity of the approximation and therefore reduces the error.

4.3.2 *Isotropic approximations for anisotropic propagation*

In many cases, computational FZTW models are based on isotropic wave propagation. Here, we investigate the errors that are induced by approximating an anisotropic velocity model with an isotropic approximation. A velocity model with transverse-isotropy is defined by the five parameters (α_0, β_0, ϵ, δ, γ) as described in Section 4.1, whereas an isotropic velocity model has only two parameters (α, β).

The high angle approximations of eqs (1) used for the F_R mode are $\beta = \beta_0$ and $\alpha = \alpha_0\sqrt{1+2\epsilon}$. The percentual errors in the group velocity with this approximation are shown in Fig. 8. As expected, when comparing the second and third rows of Fig. 8, it can be seen that the isotropic approximation is worse than the $\delta = \epsilon/2$ approximation.

The high angle approximation for the F_L mode is $\beta = \beta_0\sqrt{1+2\gamma}$. To test the feasibility of this approximation, we compute a simulation with $\gamma = 0.15$ in the country-rock, while $\gamma = 0.3$ is the maximum value in the fault zone. We find that, as with F_R, these approximations are worse for greater velocity contrasts and for velocity models that have a larger cross-section of the fault zone at the minimum velocity. The errors of these approximations can be seen in Fig. 9. This shows that in many cases, depending on required accuracy, the isotropic approximation can be used to simplify models.

5 IMPLICATIONS FOR MODELLING FZTWs

Imaging using FZTWs often produces non-unique solutions (Ben-Zion 1998). This means that the imaging process is sensitive to measurement and modelling errors (Tarantola 2004). FZTWs produced from a three-layer model have a lower minimum group velocity than a fault zone with a smoothly decaying velocity model. Therefore, making a three-layer approximation for the purposes of estimating fault-zone parameters could lead to underestimation of the velocity contrast, underestimation of fault-zone depth, or overestimation of fault-zone width. This means that, in order to obtain more accurate constraints on variations with depth (e.g. Ben-Zion *et al.* 2003), the across-fault profile should be considered carefully.

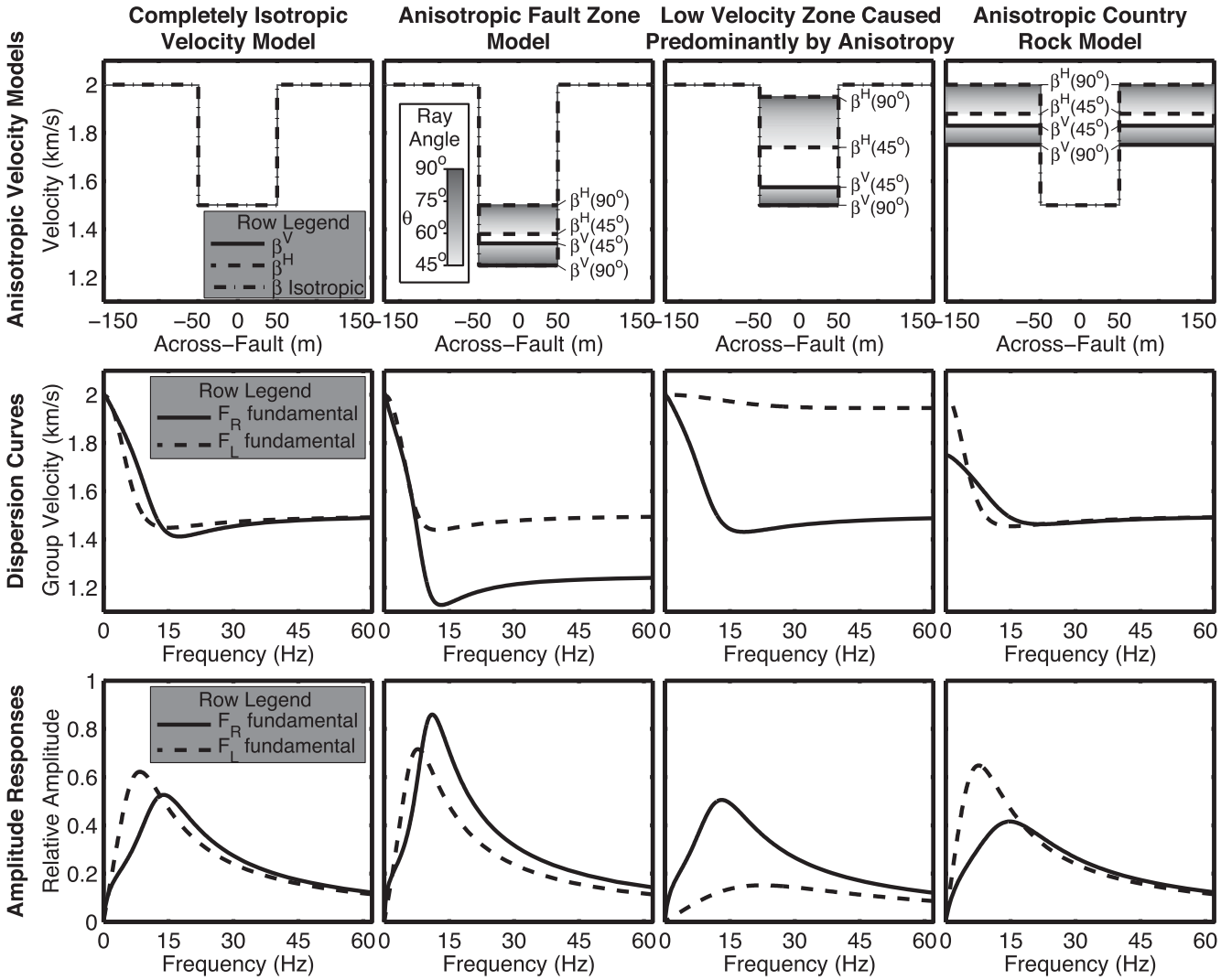

Figure 7. Investigates the effect of several different anisotropic fault-zone models. Where each column shows the investigations of the different velocity models. The first row gives the anisotropic velocity model for the SH (β^{H}) and SV (β^{V}) waves. The grey scales in each figure shows the velocities for different propagation angles. The colour scale for these propagation angles are given in the second figure where $\theta = 90^{\circ}$ is for a ray traveling in the waveguide parallel direction and $\theta = 0^{\circ}$ is in the waveguide normal direction although, we only show the range $45^{\circ} \leq \theta \leq 90^{\circ}$. The second row shows the F_L and F_R dispersion curves of the fundamental. The third row shows the amplitude response from the fundamental of F_R transverse component and the F_L wave. An infinite line source is used and the source and receiver are both located 25 m from the centre of the fault. The scale of velocity amplitude is arbitrary. The first column is an isotropic velocity model to be used for comparison. The second column is a situation that could arise from fault-aligned fractures or bedding in the fault zone. The third column shows a situation where the waveguide is mostly caused by anisotropy from fault-aligned fractures or bedding. The fourth column shows the effect of fault-aligned fractures or bedding in the country-rock but not in the fault zone. Only the three-layer velocity model and the fundamental harmonic is shown. These results, however, are similar to other velocity models and harmonics. It can be seen that anisotropy in the fault zone causes F_R to have a greater amplitude response and lower minimum group velocity than F_L. This leads to greater amplitude F_R with longer wave trains. The country-rock having anisotropy has the opposite effect.

Many complementary sources of information can be used to improve constraints on fault-zone properties and hence inform FZTW inversions. At the surface, geologic information can be used to understand the rock types and properties and the across-fault profile (e.g. Fagereng & Toy 2011; Faulkner *et al.* 2011). Further near-surface information of velocity profiles can be obtained by high resolution body wave tomography and laboratory measurements of rock (e.g. Rempe *et al.* 2013). Drilling into faults provides good characterization of a fault-zone cross-section from extracted samples and geophysical well logging (e.g. Jeppson *et al.* 2010; Zoback *et al.* 2011; Townend *et al.* 2013). To cover a larger volume in the upper few kilometres, seismic fault-zone trapped noise has been effectively utilized to obtain estimates of fault-zone properties (Hillers *et al.* 2014; Ben-Zion *et al.* 2015; Liu *et al.* 2015; Hillers & Campillo 2016; Roux *et al.* 2016). Excluding some very deep drilling projects the above methods are unable to image fault zones at greater than a few km deep. At these depths FZTWs from micro earthquakes can be used. Observations from body wave tomography can be used to constrain the country rock velocities (e.g. Eberhart-Phillips & Michael 1993; Eberhart-Phillips & Bannister 2002).

Recently very dense arrays of seismometers have been placed on top of and around fault zones (Cochran *et al.* 2009; Lin *et al.* 2013; Ben-Zion *et al.* 2015). This data allows seismic noise studies (e.g. Hillers *et al.* 2014) as well as a greater number of recordings of

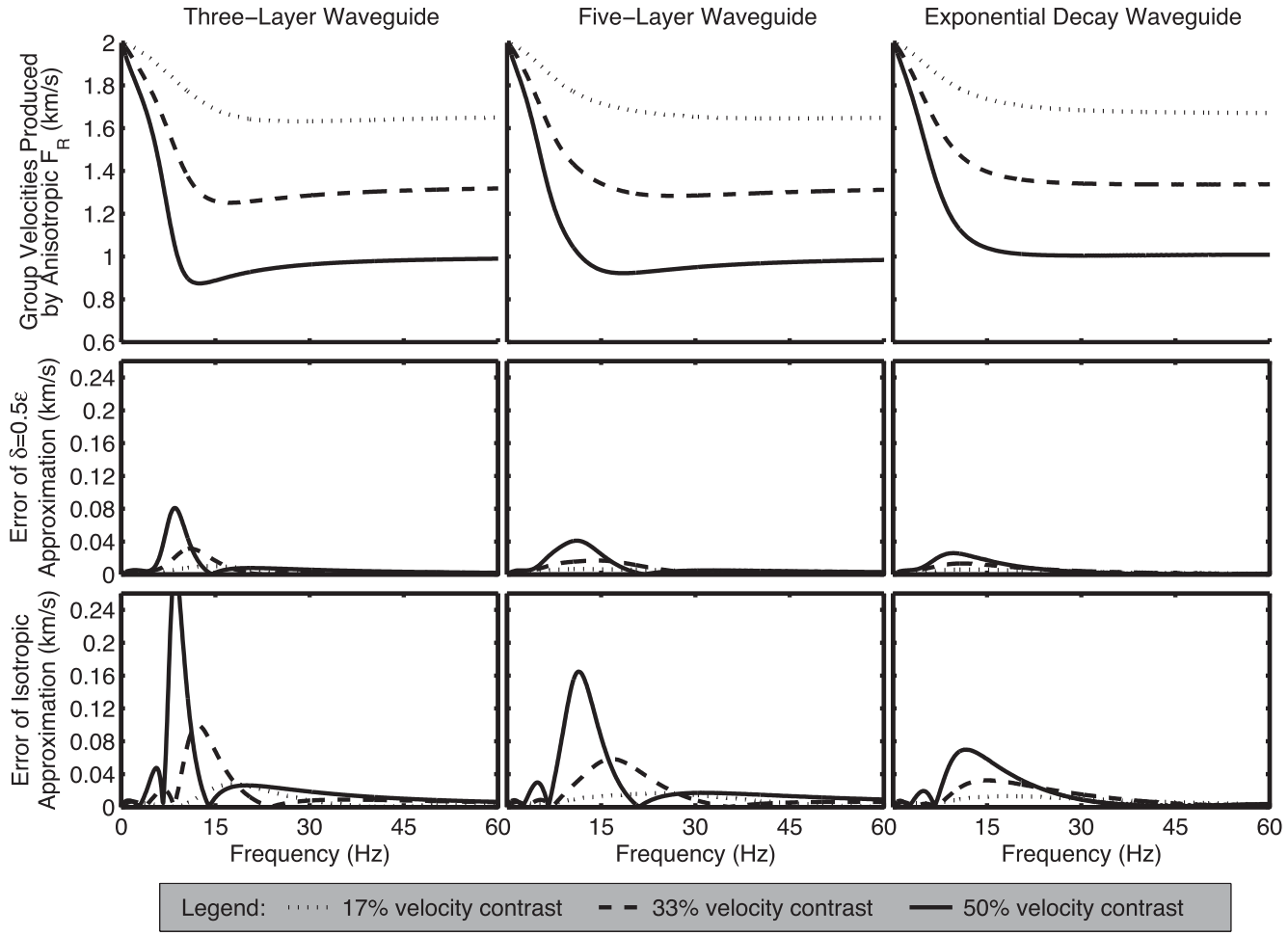

Figure 8. The top row shows the dispersion curve produced by setting the anisotropy parameters $\epsilon = 0.15$ in the country-rock, $\epsilon = 0.3$ is the maximum value in the fault zone and $\delta = \epsilon/4$. The three different curve sets all have maximum *SV*-wave velocities in the waveguide parallel direction of 2 km s^{-1}, the top curve set has a minimum *S*-wave velocity in the waveguide parallel direction of 1.67 km s^{-1} and the middle and bottom curve sets have 1.33 km s^{-1} and 1 km s^{-1} respectively. More information on the velocity models can be seen in Fig. 2. The middle row shows the percentual difference between the group velocity when approximating the anisotropy parameter δ with $\delta = \epsilon/2$. The bottom row shows the percentual errors in the group velocity when approximating the anisotropic velocity model with an isotropic model that has the same velocities in the fault-parallel direction. It can be seen that the errors increase for greater velocity contrasts and for velocity models that have a larger cross-section of the fault zone at the minimum velocity.

FZTWs. In order to identify the across-fault velocity model from a seismometer array it would be better to have a higher density of seismometers near the boundary (effective width) of the fault zone. This is because this is where the variation between the three-layer and gradational fault-zone waveforms is greatest as can be seen in the waveguide eigenvectors in Fig. 5. In addition, this location is where the amplitude information would provide the greatest constraints on fault-zone width as that is where the eigenvectors are changing the fastest. This spacing should, however, be weighed up against the fact that the FZTWs have lower amplitude near the fault-zone boundary and so the signal to noise ratio will be less. Poor signal to noise ratios may make it difficult to accurately identify the type of across-fault velocity model from FZTW data alone. Hence independent insight about the character of the fault zone and its boundaries, for example, from geology, would help to identify the best across fault velocity model type to use for the estimation of large scale fault-zone properties such as velocity contrast and width.

Additionally the across-fault velocity profile may be able to be identified by looking at the dispersion information. This would require a recording of a FZTW that has a large frequency range (e.g. 2–30 Hz) and the signal to noise ratio is small enough such that it can be identified that there isn't an Airy phase. This could potentially be achieved from a near surface explosion to borehole recording.

Our results suggest that the amplitude information of FZTWs is significantly affected by attenuation, source receiver orientation and focal mechanisms, as well as the elastic properties of the fault zone and country rock. The dispersion information is, however, primarily affected only by the rock velocities and densities. Therefore, when modelling fault-zone properties, the number of parameters can be reduced by using dispersion information only. This abstraction is already readily used in FZTW studies (e.g. Wu *et al.* 2010; Wu & Hole 2011). We believe that it is most useful when the amplitude information is not going to offer significant information on rock properties. Such a situation may occur when uncertainty in source receiver orientation and location as well as focal mechanisms leads to significant uncertainty in to the frequency dependent energy of the generated FZTW.

The anisotropic investigations have shown that the F_L and F_R FZTW properties are dominated by the fault-parallel *S*-wave

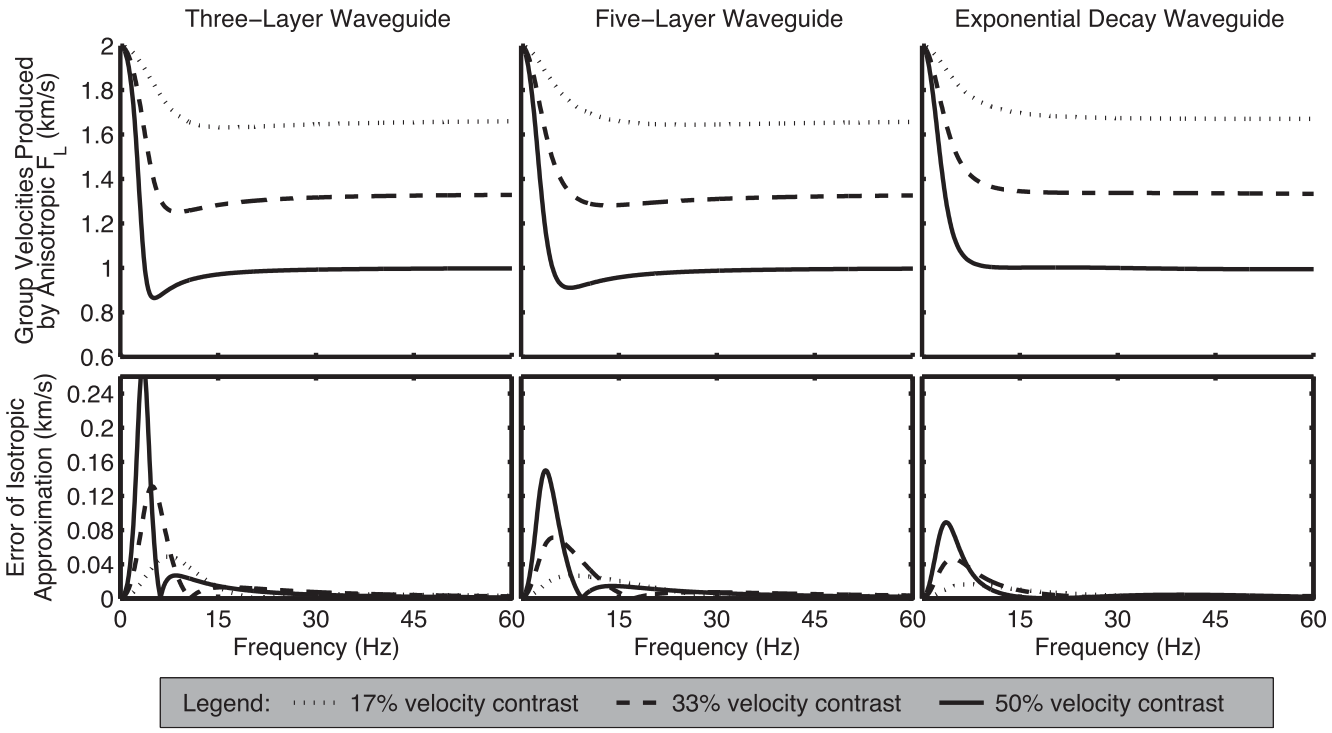

Figure 9. The top row shows the dispersion curve produced by setting the anisotropy parameters $\gamma = 0.15$ in the country-rock while $\gamma = 0.3$ is the maximum value in the fault zone. The three different curve sets all have maximum *SH*-wave velocities in the waveguide parallel direction of 2 km s^{-1}, the top curve set has a minimum *S*-wave velocity in the waveguide parallel direction of 1.67 km s^{-1} and the middle and bottom curve sets have 1.33 km s^{-1} and 1 km s^{-1} respectively. More information on the velocity models can be seen in Fig. 2. The bottom row shows the percentual difference between the group velocity when approximating the anisotropic velocity model with an isotropic model that has the same velocities in the fault-parallel direction.

velocities. These fault-parallel velocities are different for F_L and F_R. In many cases when modelling FZTWs, isotropic approximations may be made despite the knowledge that there is actually transverse-isotropy. When this is done the *S*-wave velocity for F_L and F_R should be considered to be independent.

This study suggests that a good way to estimate the degree of transverse anisotropy in a fault zone is from the travel time difference between the F_L and F_R waves. This is in a similar fashion to how anisotropy is estimated in surface waves (e.g. Montagner 1985; Hadiouche *et al.* 1989; Gaherty 2004) and the travel time difference is almost entirely caused by anisotropy. The only other influences on this travel time difference is likely to be caused by refraction of FZTWs in a 3-D velocity model (Wu & Hole 2011) or more general anisotropy. In the case of high anisotropy, one type of FZTW will have a significantly lower amplitude and may not be clearly observable in the wave-train over the *S*-wave noise. However, the loss of one type of FZTW could also occur due to source mechanisms.

6 CONCLUSIONS

Analysis of synthetic dispersion curves and amplitude responses for F_L and F_R type FZTWs in different transversally isotropic 1-D elastic models explored the potential effects of more realistic fault-zone structures. In particular, a smooth exponentially decaying velocity model has a qualitatively different dispersion curve to a three-layer model, the main differences being that there is no Airy phase and that the FZTW train is shorter with a smaller amplitude. Because of this difference in FZTW travel time, we would expect FZTW inversions that approximate a gradational velocity model with three-layers to under estimate the fault-zone velocity. In addition to this, analysis of the waveguide trapped modes shows that the radial component of the F_R is smaller than the transverse component for most realistic fault-zone velocity models and that moving the source or receiver away from the fault has an effect similar to attenuation, in that higher frequencies are lost first. Analysis of transverse anisotropy has shown that fault-aligned fractures and bedding in the fault zone will cause an increase in the F_R amplitude and wave-train length compared to F_L. On the other hand, transverse-isotropy in the country-rock reduces the F_R amplitude and wave-train length compared to F_L. We also investigated how well a transversely isotropic model can be approximated by a fully isotropic velocity model. It was found that in the case of a low velocity contrast, a transversally isotropic fault zone can be approximated by an isotropic velocity model where the isotropic velocities are equal to the anisotropic velocities in the direction parallel to the fault. It is important to note that the isotropic approximation is different for F_L and F_R mode guided waves in the same transversely isotropic waveguide.

ACKNOWLEDGEMENTS

The authors are grateful for funding provided from the Marsden Fund administered by the Royal Society of New Zealand. The authors would also like to thank Ruanui Nicholson and Owen Dillon for helpful comments and support in the preparation of this manuscript.

REFERENCES

Aki, K. & Richards, P.G., 2009. *Quantitative Seismology,* 2nd edn, University Science Books.

Ali, A., Shahraini, A. & Jakobsen, M., 2011. Improved characterization of fault zones by quantitative integration of seismic and production data, *J. Geophys. Eng.,* **8**(2), 259–274.

Allam, A., Tape, C. & Ben-Zion, Y., 2015. Finite-frequency sensitivity kernels of seismic waves to fault zone structures, *Geophys. J. Int.,* **203**(3), 2032–2048.

Ben-Zion, Y., 1990. The response of two half spaces to point dislocations at the material interface, *Geophys. J. Int.,* **101,** 507–528.

Ben-Zion, Y., 1998. Properties of seismic fault zone waves and their utility for imaging low-velocity structures, *J. geophys. Res.,* **103,** 12 567–12 585.

Ben-Zion, Y. & Aki, K., 1990. Seismic radiation from an SH line source in a laterally heterogeneous planar fault zone, *Bull. seism. Soc. Am.,* **80,** 971–994.

Ben-Zion, Y. & Ampuero, J.-P., 2009. Seismic radiation from regions sustaining material damage, *Geophys. J. Int.,* **178**(3), 1351–1356.

Ben-Zion, Y. & Malin, P.E., 1991. San Andreas fault zone head waves near Parkfield, California, *Science,* **251**(5001), 1592–1594.

Ben-Zion, Y. & Sammis, C.G., 2003. Characterization of fault zones, *Pure appl. Geophys.,* **160**(3–4), 677–715.

Ben-Zion, Y., Katz, S. & Leary, P., 1992. Joint inversion of fault zone head waves and direct *P* arrivals for crustal structure near major faults, *J. geophys. Res.,* **97**(B2), 1943–1951.

Ben-Zion, Y. *et al.*, 2003. A shallow fault-zone structure illuminated by trapped waves in the Karadere–Duzce branch of the North Anatolian Fault, Western Turkey, *Geophys. J. Int.,* **152**(3), 699–717.

Ben-Zion, Y. *et al.*, 2015. Basic data features and results from a spatially dense seismic array on the San Jacinto fault zone, *Geophys. J. Int.,* **202**(1), 370–380.

Berryman, J.G., 1979. Long-wave elastic anisotropy in transversely isotropic media, *Geophysics,* **44**(5), 896–917.

Blum, T.E., Adam, L. & van Wijk, K., 2013. Noncontacting benchtop measurements of the elastic properties of shales, *Geophysics,* **78**(3), C25–C31.

Boese, C.M., Townend, J., Smith, E. & Stern, T., 2012. Microseismicity and stress in the vicinity of the Alpine Fault, central Southern Alps, New Zealand, *J. geophys. Res.,* **117,** B02302, doi:10.1029/2011JB008460.

Buchanan, D.J., Jackson, P.J. & Davis, R., 1983. Attenuation and anisotropy of channel waves in coal seams, *Geophysics,* **48**(2), 133–147.

Calderoni, G., Giovambattista, R.D., Vannoli, P., Pucillo, S. & Rovelli, A., 2012. Fault-trapped waves depict continuity of the fault system responsible for the 6 April 2009 Mw 6.3 L'Aquila earthquake, central Italy, *Earth planet. Sci. Lett.,* **323–324,** 1–8.

Chapman, C., 2004. *Fundamentals of Seismic Wave Propagation,* Cambridge Univ. Press.

Chester, F.M., Evans, J.P. & Biegel, R.L., 1993. Internal structure and weakening mechanisms of the San Andreas Fault, *J. geophys. Res.,* **98**(B1), 771–786.

Cochran, E. & Vidale, J.E., 2001. Seismic anisotropy of the Hector Mine fault zone, in *EOS, Trans. Am. geophys. Un.,* **82,** S41A.

Cochran, E.S., Li, Y.-G., Shearer, P.M., Barbot, S., Fialko, Y. & Vidale, J.E., 2009. Seismic and geodetic evidence for extensive, long-lived fault damage zones, *Geology,* **37**(4), 315–318.

den Hartog, S.A., Peach, C.J., de Winter, D.M., Spiers, C.J. & Shimamoto, T., 2012. Frictional properties of megathrust fault gouges at low sliding velocities: new data on effects of normal stress and temperature, *J. Struct. Geol.,* **38,** 156–171.

Dor, O., Rockwell, T.K. & Ben-Zion, Y., 2006. Geological observations of damage asymmetry in the structure of the San Jacinto, San Andreas and Punchbowl faults in Southern California: a possible indicator for preferred rupture propagation direction, *Pure appl. Geophys.,* **163**(2), 301–349.

Eberhart-Phillips, D. & Bannister, S., 2002. Three-dimensional crustal structure in the Southern Alps region of New Zealand from inversion of local earthquake and active source data, *J. geophys. Res.,* **107**(B10), 2262, doi:10.1029/2001JB000567.

Eberhart-Phillips, D. & Michael, A.J., 1993. Three-dimensional velocity structure, seismicity, and fault structure in the Parkfield region, central California, *J. geophys. Res.,* **98**(B9), 15 737–15 758.

Eccles, J., Gulley, A., Malin, P., Boese, C., Sutherland, R. & Townend, J., 2015. Fault zone guided waves generation on the locked, late interseismic Alpine Fault, New Zealand: implications for seismogenesis, *Geophys. Res. Lett.,* **42**(14), 5736–5743.

Ellsworth, W.L. & Malin, P.E., 2011. Deep rock damage in the San Andreas Fault revealed by *P*- and *S*-type fault-zone-guided waves, *Geol. Soc. Lond. Spec. Publ.,* **359**(1), 39–53.

Ellsworth, W.L. *et al.*, 2007. Seismology inside the fault zone: Applications to fault-zone properties and rupture dynamics, *Sci. Drill.,* (Special Issue No. 1), 84–87.

Fagereng, Å. & Toy, V.G., 2011. Geology of the earthquake source: an introduction, *Geol. Soc. Lond. Spec. Publ.,* **359**(1), 1–16.

Faulkner, D., Jackson, C., Lunn, R., Schlische, R., Shipton, Z., Wibberley, C. & Withjack, M., 2010. A review of recent developments concerning the structure, mechanics and fluid flow properties of fault zones, *J. Struct. Geol.,* **32**(11), 1557–1575.

Faulkner, D.R., Mitchell, T.M., Jensen, E. & Cembrano, J., 2011. Scaling of fault damage zones with displacement and the implications for fault growth processes, *J. geophys. Res.,* **116**, B05403, doi:10.1029/2010JB007788.

Fialko, Y., Sandwell, D., Agnew, D., Simons, M., Shearer, P. & Minster, B., 2002. Deformation on nearby faults induced by the 1999 Hector Mine earthquake, *Science,* **297**(5588), 1858–1862.

Fohrmann, M., Igel, H., Jahnke, G. & Ben-Zion, Y., 2004. Guided waves from sources outside faults: an indication for shallow fault zone structure?, *Pure appl. Geophys.,* **161**(11), 2125–2137.

Gaherty, J.B., 2004. A surface wave analysis of seismic anisotropy beneath eastern North America, *Geophys. J. Int.,* **158**(3), 1053–1066.

Gulley, A.K., Kaipio, J.P., Eccles, J.D. & Malin, P.E., 2017. A numerical approach for modelling fault-zone trapped waves, *Geophys. J. Int*., in press, doi:10.1093/gji/ggx199.

Haberland, C. *et al.*, 2003. Modeling of seismic guided waves at the Dead Sea Transform, *J. geophys. Res.,* **108**, 2342, doi:10.1029/2002JB002309.

Haberland, C. *et al.*, 2007. Shallow architecture of the Wadi Araba Fault (Dead Sea Transform) from high-resolution seismic investigations, *Tectonophysics,* **432**(1–4), 37–50.

Hadiouche, O., Jobert, N. & Montagner, J.P., 1989. Anisotropy of the African continent inferred from surface waves, *Phys. Earth planet. Inter.,* **58**(1), 61–81.

Haines, S., Marone, C. & Saffer, D., 2014. Frictional properties of low-angle normal fault gouges and implications for low-angle normal fault slip, *Earth planet. Sci. Let.,* **408,** 57–65.

Hillers, G. & Campillo, M., 2016. Fault zone reverberations from cross-correlations of earthquake waveforms and seismic noise, *Geophys. J. Int.,* **204**(3), 1503–1517.

Hillers, G., Campillo, M., Ben-Zion, Y. & Roux, P., 2014. Seismic fault zone trapped noise, *J. geophys. Res.,* **119**(7), 5786–5799.

Hough, S.E., Ben-Zion, Y. & Leary, P., 1994. Fault-zone waves observed at the southern Joshua Tree earthquake rupture zone, *Bull. seism. Soc. Am.,* **84**(3), 761–767.

Hung, J.-H., Ma, K.-F., Wang, C.-Y., Ito, H., Lin, W. & Yeh, E.-C., 2009. Subsurface structure, physical properties, fault-zone characteristics and stress state in scientific drill holes of Taiwan Chelungpu Fault Drilling Project, *Tectonophysics,* **466**(3–4), 307–321.

Igel, H., Ben-Zion, Y. & Leary, P.C., 1997. Simulation of SH- and *P–SV*-wave propagation in fault zones, *Geophys. J. Int.,* **128**(3), 533–546.

Igel, H., Jahnke, G. & Ben-Zion, Y., 2002. Numerical simulation of fault zone guided waves: Accuracy and 3-D effects, *Pure appl. Geophys.,* **159**(9), 2067–2083.

Jahnke, G., Igel, H. & Ben-Zion, Y., 2006. Three-dimensional calculations of fault-zone-guided waves in various irregular structures, *Geophys. J. Int.,* **151,** 416–426.

Jeppson, T.N., Bradbury, K.K. & Evans, J.P., 2010. Geophysical properties within the San Andreas Fault Zone at the San Andreas Fault Observatory at Depth and their relationships to rock properties and fault zone structure, *J. geophys. Res.,* **115,** B12423, doi:10.1029/2010JB007563.

Johri, M., Dunham, E.M., Zoback, M.D. & Fang, Z., 2014. Predicting fault damage zones by modeling dynamic rupture propagation

and comparison with field observations, *J. geophys. Res.,* **119**(2), 1251–1272.

Kennett, B. L.N., 1983. *Seismic Wave Propagation in Stratified Media,* Cambridge Univ. Press.

Komatitsch, D. & Tromp, J., 1999. Introduction to the spectral element method for three-dimensional seismic wave propagation, *Geophys. J. Int.,* **139**(3), 806–822.

Leary, P.C., Li, Y.-G. & Aki, K., 1985. Borehole observations of fault zone trapped waves, Oroville, CA, in *EOS, Trans. Am. geophys. Un.,* **66,** 976.

Leary, P.C., Li, Y.-G. & Aki, K., 1987. Observation and modelling of fault-zone fracture seismic anisotropy–I. *P*, *SV* and *SH* travel times, *Geophys. J. R. astr. Soc.*, **91**(2), 461–484.

Lewis, M.A. & Ben-Zion, Y., 2010. Diversity of fault zone damage and trapping structures in the Parkfield section of the San Andreas Fault from comprehensive analysis of near fault seismograms, *Geophys. J. Int.,* **183**(3), 1579–1595.

Lewis, M., Peng, Z., Ben-Zion, Y. & Vernon, F., 2005. Shallow seismic trapping structure in the San Jacinto fault zone near Anza, California, *Geophys. J. Int.,* **162**(3), 867–881.

Lewis, M.A., Ben-Zion, Y. & McGuire, J.J., 2007. Imaging the deep structure of the San Andreas Fault south of Hollister with joint analysis of fault zone head and direct P arrivals, *Geophys. J. Int.,* **169**(3), 1028–1042.

Li, Y.-G. & Leary, P., 1990. Fault zone seismic trapped waves, *Bull. seism. Soc. Am.,* **80,** 1245–1271.

Li, Y.-G. & Vidale, J.E., 1996. Low-velocity fault-zone guided waves: numerical investigations of trapping efficiency, *Bull. seism. Soc. Am.,* **86,** 371–378.

Li, Y.-G. & Vernon, F., 2001. Characterization of the San Jacinto fault zone near Anza, California, by fault zone trapped waves, *J. geophys. Res.,* **106**(B12), 30 671–30 688.

Li, Y.-G. & Malin, P.E., 2008. San Andreas Fault damage at SAFOD viewed with fault-guided waves, *Geophys. Res. Lett.,* **35,** L08304, doi:10.1029/2007GL032924.

Li, Y.-G., Leary, P.C. & Aki, K., 1987. Observation and modelling of fault-zone fracture seismic anisotropy–II. *P*-wave polarization anomalies, *Geophys. J. R. astr. Soc.,* **91,** 485–492.

Li, Y.-G., Leary, P., Aki, K. & Malin, P., 1990. Seismic trapped modes in the Oroville and San Andreas fault zones, *Science,* **249**(4970), 763–766.

Li, Y.-G., Aki, K., Adams, D., Hasemi, A. & Lee, W. H.K., 1994. Seismic guided waves trapped in the fault zone of the Landers, California, earthquake of 1992, *J. geophys. Res.,* **99**(B6), 11 705–11 722.

Li, Y.-G., Ellsworth, W.L., Thurber, C.H., Malin, P.E. & Aki, K., 1997. Fault-zone guided waves from explosions in the San Andreas Fault at Parkfield and Cienega Valley, California, *Bull. seism. Soc. Am.,* **87**(1), 210–221.

Li, Y.-G., Aki, K., Vidale, J.E. & Alvarez, M.G., 1998. A delineation of the Nojima Fault ruptured in the M7.2 Kobe, Japan, earthquake of 1995 using fault zone trapped waves, *J. geophys. Res.,* **103**(B4), 7247–7263.

Li, Y.-G., Aki, K., Vidale, J. & Xu, F., 1999. Shallow structure of the Landers fault zone from explosion-generated trapped waves, *J. geophys. Res.,* **104**(B9), 20 257–20 275.

Li, Y.-G., Vidale, J., Aki, K. & Xu, F., 2000. Depth-dependent structure of the Landers fault zone from trapped waves generated by aftershocks, *J. geophys. Res.,* **105**(B3), 6237–6254.

Li, Y.-G., Vidale, J.E., Day, S.M. & Oglesby, D.D., 2002. Study of the 1999 M7.1 Hector Mine, California, earthquake fault plane by trapped waves, *Bull. seism. Soc. Am.,* **92**(4), 1318–1332.

Li, Y.-G., Vidale, J.E. & Cochran, E.S., 2004. Low-velocity damaged structure of the San Andreas Fault at Parkfield from fault zone trapped waves, *Geophys. Res. Lett.,* **31**(12), L12S06, doi:10.1029/2003GL019044.

Li, Y.-G., Pascale, G. P.D., Quigley, M.C. & Gravley, D.M., 2014. Fault damage zones of the M7.1 Darfield and M6.3 Christchurch earthquakes characterized by fault-zone trapped waves, *Tectonophysics,* **618**(0), 79–101.

Lin, F.-C., Li, D., Clayton, R.W. & Hollis, D., 2013. High-resolution 3D shallow crustal structure in Long Beach, California: application of ambient noise tomography on a dense seismic array, *Geophysics,* **78**(4), Q45–Q56.

Lindsey, E.O., Sahakian, V.J., Fialko, Y., Bock, Y., Barbot, S. & Rockwell, T.K., 2014. Interseismic strain localization in the San Jacinto fault zone, *Pure appl. Geophys.,* **171**(11), 2937–2954.

Liu, X., Ben-Zion, Y. & Zigone, D., 2015. Extracting seismic attenuation coefficients from cross-correlations of ambient noise at linear triplets of stations, *Geophys. J. Int.,* **203**(2), 1149–1163.

Lou, M. & Crampin, S., 1991. Dispersion of guided waves in thin anisotropic waveguides, *Geophys. J. Int.,* **107**(3), 545–555.

Malin, P.E. & Lou, M., 1996. FR waves: A second fault-guided mode with implications for fault property studies, *Geophys. Res. Lett.,* **23(24),** 3547–3550.

Michael, A.J. & Ben-Zion, Y., 1998. Challenges in inverting fault zone trapped waves to determine structural properties, in *EOS, Trans. Am. geophys. Un.,* **79,** 231.

Mitchell, T. & Faulkner, D., 2009. The nature and origin of off-fault damage surrounding strike-slip fault zones with a wide range of displacements: A field study from the Atacama Fault system, northern Chile, *J. Struct. Geol.,* **31**(8), 802–816.

Mizuno, T. & Nishigami, K., 2006. Deep structure of the Nojima Fault, southwest Japan, estimated from borehole observations of fault-zone trapped waves, *Tectonophysics,* **417**(3–4), 231–247.

Mizuno, T., Nishigami, K., Ito, H. & Kuwahara, Y., 2004. Deep structure of the Mozumi-Sukenobu Fault, central Japan, estimated from the subsurface array observation of fault zone trapped waves, *Geophys. J. Int.,* **159**(2), 622–642.

Mizuno, T., Kuwahara, Y., Ito, H. & Nishigami, K., 2008. Spatial variations in fault-zone structure along the Nojima Fault, central Japan, as inferred from borehole observations of fault-zone trapped waves, *Bull. seism. Soc. Am.,* **98**(2), 558–570.

Montagner, J.-P., 1985. Seismic anisotropy of the Pacific Ocean inferred from long-period surface waves dispersion, *Phys. Earth planet. Inter.,* **38**(1), 28–50.

Mooney, W. & Ginzburg, A., 1986. Seismic measurements of the internal properties of fault zones, *Pure appl. Geophys.,* **124**(1–2), 141–157.

Nakamura, T. & Takenaka, H., 2006. A numerical analysis of seismic waves for an anisotropic fault zone, *Earth Planets Space,* **58**(5), 569–582.

Peng, Z. & Gomberg, J., 2010. An integrated perspective of the continuum between earthquakes and slow-slip phenomena, *Nat. Geosci.,* **2**(9), 599–607.

Peng, Z., Ben-Zion, Y., Michael, A. & Zhu, L., 2003. Quantitative analysis of seismic fault zone waves in the rupture zone of the 1992 Landers, California, earthquake: evidence for a shallow trapping structure, *Geophys. J. Int.,* **155**(3), 1021–1041.

Rempe, M., Mitchell, T., Renner, J., Nippress, S., Ben-Zion, Y. & Rockwell, T., 2013. Damage and seismic velocity structure of pulverized rocks near the San Andreas Fault, *J. geophys. Res.,* **118**(6), 2813–2831.

Roux, P., Moreau, L., Lecointre, A., Hillers, G., Campillo, M., Ben-Zion, Y., Zigone, D. & Vernon, F., 2016. A methodological approach towards high-resolution surface wave imaging of the San Jacinto Fault Zone using ambient-noise recordings at a spatially dense array, *Geophys. J. Int.,* **206**(2), 980–992.

Savage, H.M. & Brodsky, E.E., 2011. Collateral damage: evolution with displacement of fracture distribution and secondary fault strands in fault damage zones, *J. geophys. Res.,* **116,** B03405, doi:10.1029/2010JB007665.

Tarantola, A., 2004. *Inverse Problem Theory and Methods for Model Parameter Estimation,* Society for Industrial and Applied Mathematics.

Thomsen, L., 1986. Weak elastic anisotropy, *Geophysics,* **51**(10), 1954–1966.

Townend, J., Sutherland, R., Toy, V.G., Eccles, J.D., Boulton, C., Cox, S.C. & McNamara, D., 2013. Late-interseismic state of a continental plate-bounding fault: petrophysical results from DFDP-1 wireline logging and core analysis, Alpine Fault, New Zealand, *Geochem. Geophys. Geosyst.,* **14**(9), 3801–3820.

Toy, V.G. *et al.*, 2015. Fault rock lithologies and architecture of the central Alpine fault, New Zealand, revealed by DFDP-1 drilling, *Lithosphere,* **7**(2), 155–173.

Tromp, J., Tape, C. & Liu, Q., 2005. Seismic tomography, adjoint methods, time reversal and banana-doughnut kernels, *Geophys. J. Int.,* **160**(1), 195–216.

Weatherley, D.K. & Henley, R.W., 2013. Flash vaporization during earthquakes evidenced by gold deposits, *Nat. Geosci.,* **6,** 294–298.

Wu, J., 2008. New constraints on fault-zone structure from seismic guided waves, *PhD thesis,* Virginia Polytechnic Institute and State University.

Wu, J. & Hole, J.A., 2011. Refraction of fault-zone guided seismic waves, *Bull. seism. Soc. Am.,* **101**(4), 1674–1682.

Wu, J., Hole, J.A., Snoke, J.A. & Imhof, M.G., 2008. Depth extent of the fault-zone seismic waveguide: effects of increasing velocity with depth, *Geophys. J. Int.,* **173**(2), 611–622.

Wu, J., Hole, J.A. & Snoke, J.A., 2010. Fault zone structure at depth from differential dispersion of seismic guided waves: evidence for a deep waveguide on the San Andreas Fault, *Geophys. J. Int.,* **182**(1), 343–354.

Xu, S., Ben-Zion, Y. & Ampuero, J.-P., 2012. Properties of inelastic yielding zones generated by in-plane dynamic ruptures–II. Detailed parameter-space study, *Geophys. J. Int.,* **191**(3), 1343–1360.

Yang, H., 2015. Recent advances in imaging crustal fault zones: a review, *Earthq. Sci.,* **28**(2), 151–162.

Yang, H. & Zhu, L., 2010. Shallow low-velocity zone of the San Jacinto fault from local earthquake waveform modelling, *Geophys. J. Int.,* **183**(1), 421–432.

Yang, H., Zhu, L. & Cochran, E.S., 2011. Seismic structures of the calico fault zone inferred from local earthquake travel time modelling, *Geophys. J. Int.,* **186**(2), 760–770.

Yang, H., Li, Z., Peng, Z., Ben-Zion, Y. & Vernon, F., 2014. Low-velocity zones along the San Jacinto Fault, Southern California, from body waves recorded in dense linear arrays, *J. geophys. Res.,* **119**(12), 8976–8990.

Zhang, J. & Gerstoft, P., 2014. Local-scale cross-correlation of seismic noise from the calico fault experiment, *Earthq. Sci.,* **27**(3), 311–318.

Zoback, M., Hickman, S. & Ellsworth, W., 2011. Scientific drilling into the San Andreas fault zone–an overview of SAFOD's first five years, *Sci. Drill.,* **11,** 14–28.